

## Chapter

# Artificial Synapses Based on Atomic/Molecular Layer Deposited Bilayer-Structured Memristive Thin Films

*Chang Liu, Lin Zhu, Lai-Guo Wang and Ai-Dong Li*

## Abstract

This chapter deals with several kinds of ultrathin bilayer-structured memristors, such as Pt/Al<sub>2</sub>O<sub>3</sub>/HfO<sub>2</sub>/TiN, Pt/HfO<sub>2</sub>/HfO<sub>x</sub>/TiN, Pt/TiO<sub>2</sub>/Ti-based maleic acid (Ti-MA)/TaN, among which the asymmetric memristive functional layers were designed and prepared by atomic layer deposition (ALD) or molecular layer deposition (MLD) technique. These bilayer memristors exhibit a typical bipolar resistive switching characteristic, in accord with the space charge limited current model. Some important biologic synaptic functions have been achieved, including nonlinear transmission characteristics, spike-timing-dependent plasticity, short-/long-term plasticity, paired-pulse facilitation, and conditioned reflex. The mechanism of bilayer memristive device has been proposed based on oxygen vacancies migration/diffusion model. Above all the ultrathin bilayer memristors fabricated by low temperature ALD/MLD are one competitive candidate for neuromorphic simulation and flexible electronic applications.

**Keywords:** memristor, atomic layer deposition, bilayer, synapse, mechanism

## 1. Introduction

The memristor concept was first proposed as the fourth fundamental passive circuit element by Chua in 1971 based on the completeness of the circuit theory, which indicates the relationship between magnetic flux and charge [1, 2]. After thirty seven years, Strukov et al. eventually found the missing memristor in studying TiO<sub>2</sub> cross-arrays in 2008 [2]. This draws the extensive and intensive attention from the academia and the industry. Memristor is a two-terminal electrical device whose resistance can be tuned by changing the flux or charge through it. Memristor possesses a lot of advantages, e.g., simple device architecture, high energy efficiency, better compatibility with semiconductor industry, and high integration density.

A neural synapse, as the basic unit of learning and memory in the brain, plays a critical role in biological neural networks. Electronic synapses are utilized to emulate the bio-synapses' functions. Some researches on synapse simulation have been reported by adjusting synaptic weights so as to make an effective bio-inspired computing system [3–6]. Nevertheless, most work chose transistors and capacitors

to realize artificial synapse, which produced high energy consumption at high integration density and limited the programming running. The new memristor has nonlinear transfer characteristics similar to the bio-synapse and is regarded as the closest to the synaptic device [4].

Although various materials and structures exhibit memristive behavior, almost all the memristor systems are based on the structural asymmetry [7, 8]. For example, in the metal-insulator-metal (MIM) structure, the defects such as oxygen vacancy or active ions in the insulator layer can induce structural asymmetry under the action of the external field, or when one of the metal electrodes is active. Therefore, the asymmetric bilayer-structured memristors play a crucial role in constructing artificial neural networks for brain-inspired applications.

Atomic layer deposition (ALD) is a kind of commercial technology compatible with semiconductor processing. It shows unusual advantages in controllable fabrication of nano-laminate thin films due to its unique sequential self-limiting surface reaction mechanism at low growth temperature [9, 10]. In early 2001 ALD has been known as candidate technology preferred for semiconductor industry along with metalorganic chemical vapor deposition (MOCVD) and plasma-enhanced CVD by the international technology roadmap for semiconductors (ITRS) [11]. ALD has become one of the most competitive deposition techniques for microelectronics and nanotechnology owing to sub-nanometer thickness control, large-area uniformity, excellent three-dimensional conformality, and good reproducibility. Thin films with low defect density can be prepared by ALD even at room temperature (RT) with plasma assistance [12]. Evidently, low temperature or RT ALD technology can greatly widen the flexible substrate choice range, showing exciting potentials in flexible electronic device fabrication. Molecular layer deposition (MLD) can be regarded as the subtype of ALD due to the molecular nature of the deposition process, suitable for growth of organic-inorganic hybrid materials [13].

In this section, we fabricated several synaptic devices of asymmetric bilayer-structured ultrathin memristors by atomic layer deposition (ALD) and molecular layer deposition (MLD), such as Pt/ $\text{AlO}_x$ / $\text{HfO}_x$ /TiN, Pt/ $\text{HfO}_2$ / $\text{HfO}_x$ /TiN, Pt/ $\text{TiO}_2$ /Ti-based maleic acid (Ti-MA)/TaN. Some biological synapse-like functions of long-/short-term plasticity (LTP and STP), spike-timing-dependent plasticity (STDP), and paired-pulse facilitation (PPF) have been achieved simultaneously. A memristive mechanism of an asymmetric bilayer-structured synaptic device has been proposed to explain synaptic plasticity based on the oxygen vacancy migration/diffusion model.

## 2. Bilayer-structured ultrathin memristors

### 2.1 Fabrication processing

Asymmetric bilayer-structured ultrathin memristor based on Pt/A/B/TiN or TaN was fabricated on  $\text{SiO}_2/\text{Si}$  substrates by thermal-ALD (TALD), MLD and plasma-enhanced ALD (PEALD), as illustrated in **Figure 1a**. Herein A and B act as asymmetric memristive functional layer, PEALD TiN or sputtered TaN as bottom electrode, sputtered Pt as top electrode with a spot size in diameter of 150  $\mu\text{m}$ . **Table 1** gives several typical bilayer ultrathin memristors and their architectures. The related deposition conditions have been listed in **Table 2**, including used metal precursors and reactants, source temperature and deposition temperature, and growth per cycle (GPC).

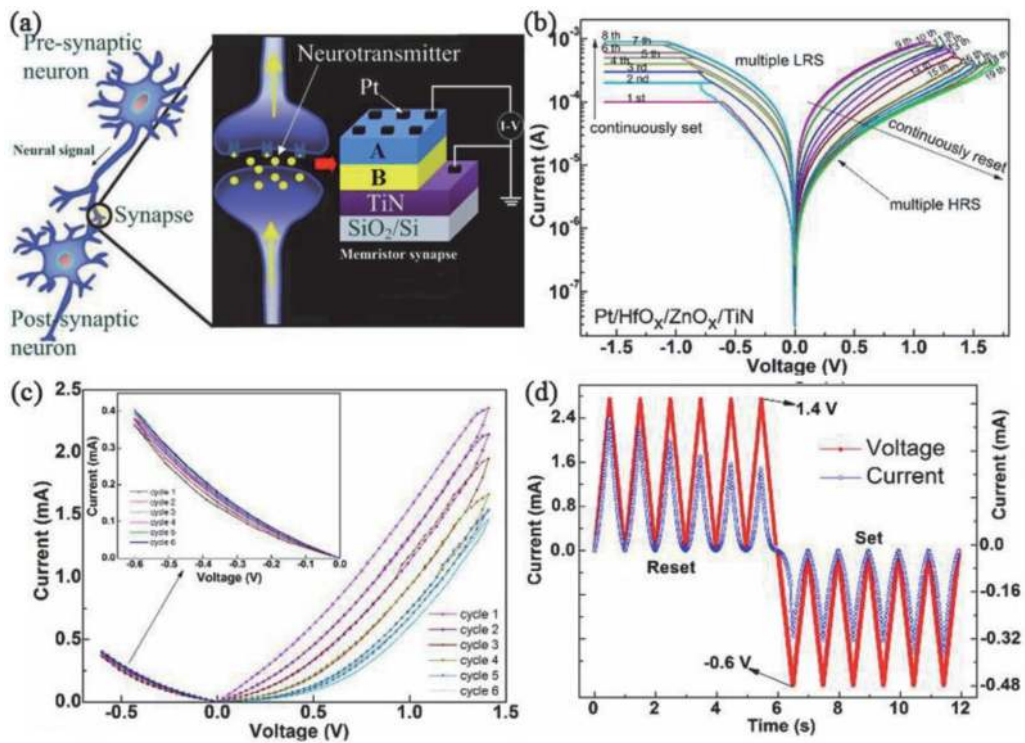


**Figure 1.** (a) Diagram of the asymmetric bilayer-structured ultrathin memristor. (b)  $I$ - $V$  characteristics of the Pt/HfO<sub>x</sub>/ZnO<sub>x</sub>/TiN synapse device measured by a modified DC double ramp sweep. The sweep sequence is denoted by the number. (c)  $I$ - $V$  characteristics of the memristor at positive and negative bias voltages. The voltage sweep range is from 0 to 1.4 (−0.6) V then back to 0 V, and the time for a sweep cycle is 1 s. the device conductivity continuously decreases or increases during the positive or negative voltage sweeps. (d) the curves of voltage and current versus time, which are plotted from the data in (c) [15].

Device structure	A (thickness)	B (thickness)
Pt/HfO <sub>x</sub> /ZnO <sub>x</sub> /TiN	HfO <sub>x</sub> (5 nm)	ZnO <sub>x</sub> (5 nm)
Pt/AlO <sub>x</sub> /HfO <sub>x</sub> /TiN	AlO <sub>x</sub> (5 nm)	HfO <sub>x</sub> (5 nm)
Pt/TiO <sub>2</sub> /Ti-MA/TaN	Ti-MA (4 nm)	TiO <sub>2</sub> (4 nm)

**Table 1.** Several typical bilayer-structured ultrathin memristors and their architectures.

	Material	Metal precursor	Precursor temperature	Reactant	Deposition temperature	GPC (Å/cycle)
TALD	HfO <sub>2</sub>	TEMAH	155°C	H <sub>2</sub> O	250°C	1
	AlO <sub>x</sub>	TMA	RT	H <sub>2</sub> O	250°C	1
	ZnO <sub>x</sub>	DEZ	RT	H <sub>2</sub> O	250°C	1.3
	TiO <sub>2</sub>	TiCl <sub>4</sub>	RT	H <sub>2</sub> O	250°C	0.3
PEALD	HfO <sub>x</sub>	TEMAH	155°C	H <sub>2</sub> plasma	250°C	1
	TiN	TiCl <sub>4</sub>	RT	NH <sub>3</sub> plasma	400°C	0.5
MLD	Ti-MA	TiCl <sub>4</sub>	RT	MA(135°C)	160°C	1.4

**Table 2.** Deposition conditions of asymmetric functional layers in memristors prepared by TALD/PEALD/MLD. Here TEMAH, TMA, DEZ, and MA refer to Hf[N(C<sub>2</sub>H<sub>5</sub>)CH<sub>3</sub>]<sub>4</sub>, Al(CH<sub>3</sub>)<sub>3</sub>, Zn(C<sub>2</sub>H<sub>5</sub>)<sub>2</sub>, maleic acid, respectively.

## 2.2 Electrical performances and synaptic functions

The electrical properties were measured under DC sweep and pulse modes using semiconductor parameter analyzer on probe station. The bottom electrode of memristors was set on ground and all the voltage signals were applied to the top electrode. The asymmetric bilayer ultrathin memristors were exploited to mimic some important synaptic functions such as long-term potentiation/depression, the transition from STP to LTP, PPF and STDP.

### 2.2.1 TiN/ZnO<sub>x</sub>/HfO<sub>x</sub>/Pt inorganic memristor

The  $I$ - $V$  curves of Pt/HfO<sub>x</sub>/ZnO<sub>x</sub>/TiN inorganic memristor are plotted in **Figure 1b** under a modified DC double sweep. To mimic the functions of a nerve synapse, one multiple-state resistances should be obtained in bilayer memristor. A continuous set or reset process was performed by successive increasing the compliance from 0.1 to 1.0 mA at an interval of 0.1 mA or altering the reset voltage from 1.0 to 1.7 V at an interval of 0.05 V. 8 low resistance states (LRS) and 11 distinguishable high resistance states (HRS) are observed during consecutive set and reset process, respectively. Moreover the resistance can be continuously reduced or raised between multiple intermediate states without going back to the original state, which is key for electronic synapse [14]. The device conductivity decreases continuously with six easily recognized states after exerting sweep positive bias voltage from 0 to 1.4 V six times and the elevated conductivity with difficultly distinguishable ones after sweep negative pulse voltage from 0 to  $-0.6$  V (**Figure 1c** and **d**), indicating the conductance change caused by consecutive potentiating or depressing signals. It can be attributed to the dynamic change of oxygen vacancy concentration and distribution in asymmetric bilayer structure of HfO<sub>x</sub>/ZnO<sub>x</sub> under various electrical signals [15].

A series of pulse signals were designed and applied to the memristor to test the important STDP rule in the Hebbian learning theory, as seen in the insets of I and III of **Figure 2**, including the  $V-/V+ = -1.0$  V/1.0 V pulse pair signal as a presynaptic and postsynaptic spike with the 3 s interval time. Such design can prevent from the disturbance of excitatory postsynaptic current [16]. The time interval between the final presynaptic spike and the initial postsynaptic spike is defined as the relative time of  $\Delta t$ . The relative change of the synaptic weights ( $\Delta W$ ) is defined as:

$$\Delta W = (I_2 - I_1) / I_1 \times 100\% \quad (1)$$

The initial postsynaptic or presynaptic current  $I_1$  was used as the control value. After the spike pair was applied and over for 5 min, the measured presynaptic or postsynaptic current was  $I_2$ .

The dependence of  $\Delta W$  on  $\Delta t$  of Pt/HfO<sub>x</sub>/ZnO<sub>x</sub>/TiN in **Figure 2** II and IV follows the STDP learning rule. While the presynaptic spike happens before the postsynaptic spike ( $\Delta t < 0$ ), synaptic weights enhance, indicating long-term potentiation (LTP<sub>0</sub>); while the presynaptic spike appears after the postsynaptic spike, synaptic weights become small ( $\Delta t > 0$ ), implying long-term depression (LTD). And the shorter the  $\Delta t$  between the two spikes, the larger the  $\Delta W$ . The STDP data points of memristor in **Figure 2** show evident statistical scatter, similar to the biological synapse.

In addition, Pt/HfO<sub>x</sub>/ZnO<sub>x</sub>/TiN device also exhibits the nonlinear transmission efficiency, and the transition from STP to LTP (not shown here) [15].



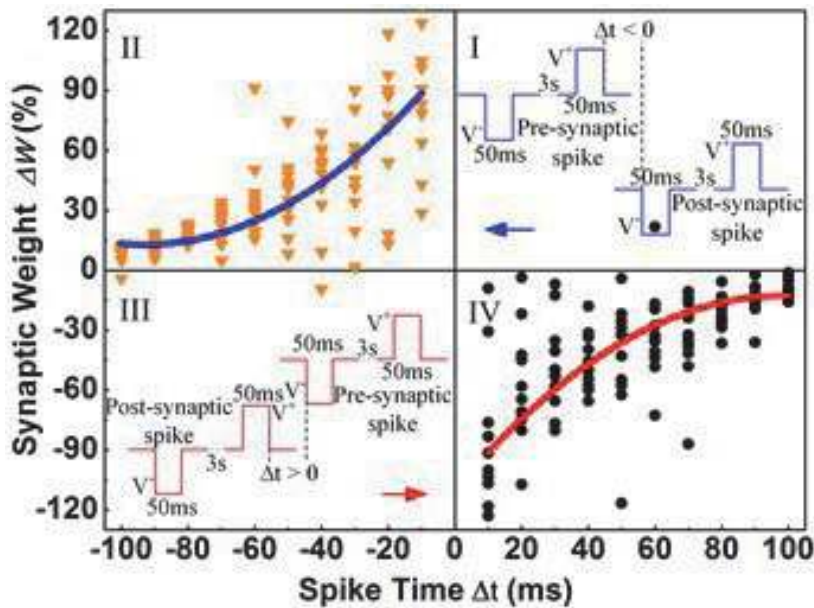


**Figure 2.** Emulation of STDP learning rule in Pt/HfO<sub>x</sub>/ZnO<sub>x</sub>/TiN memristive device—The relative change of the memristor synaptic weight ( $\Delta W$ ) versus the relative spike timing ( $\Delta t$ ). And the solid line is the fitting exponential curve to the experimental data. The insets illustrate various spike schemes. The pulse pair comprises a positive and a negative voltage pulse with amplitude of 1.0 V and width of 50 ms. The interval between the two pulses is  $\Delta t$  ms ( $t = \pm 10n$ ,  $n = 1, 2, \dots, 10$ ). The current compliance is not set in the whole emulation process. The current values are read at 0.1 V after 5 min of the spikes [15].

### 2.2.2 TiN/HfO<sub>x</sub>/AlO<sub>x</sub>/Pt inorganic memristor

The memristor device based on TiN/HfO<sub>x</sub>/AlO<sub>x</sub>/Pt can also emulate the biological synapse. Usually, the synapse operates under pulse signals rather than DC bias sweep voltage. The LTPo and LTD phenomena can be observed in Pt/AlO<sub>x</sub>/HfO<sub>x</sub>/TiN under 180 potentiating pulses (−0.5 V, 10 ms) and 180 depressing pulses (1 V, 10 ms), as shown in **Figure 3a**. The connection strength can be dynamically modulated by the consecutive external signals, determining the transfer efficiency between the electronic neurons.

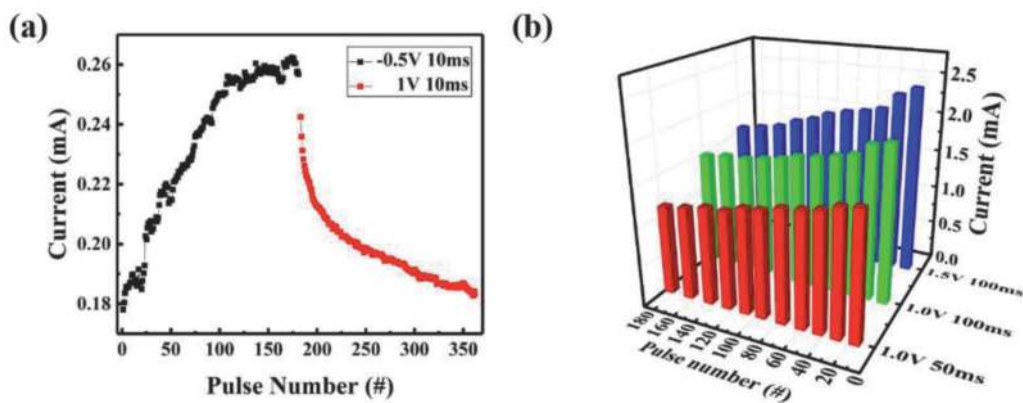


**Figure 3.** Change in the response current under the influence of consecutive potentiating or depressing pulses. After pulse stimulation, a 0.1 V 100 ns reading pulse was applied to read the response current. After −0.5 V potentiating pulses, the response current gradually increases (long-term potentiation), while the response current gradually decreases after 1 V depressing pulses (long-term depression). (b) Response of a memristor device to different pulse programs [17].

Further experiments have demonstrated that a pulse signal from amplitude of 1.0–1.5 V and pulse width of 50–100 ms leads to various current responses in **Figure 3b**. That is to say, the larger pulse amplitude, the longer pulse width, and the more pulse number will produce more significant response current change, which is analogous to long-term potentiation/depression of the human brain.

Synaptic plasticity can be divided into STP and LTP according to the timelines of enhanced synaptic connections. The repeated stimulation induced STP to LTP transition is illustrated in **Figure 4**. With increasing the rehearsal pulse number ( $N = 10, 40, 70, 100, 120$ ), the resistance remaining becomes larger (**Figure 4a**). This procedure is similar to the Ebbinghaus forgetting curve related to human memory [18, 19].

An exponential decay equation was employed to depict the relaxation process:

$$M(t) = M_e + (M_0 - M_e) \exp(-t/\tau) \quad (2)$$

where  $M(t)$ ,  $M_0$ , and  $M_e$  are the memory level at time  $t$ ,  $t = 0$ , and at steady state after a long time, and  $\tau$  of the relaxation time constant. The experimental and simulation results after 70 identical pulses are shown in **Figure 4b**, containing the dependence of  $\tau$  on  $N$  in the inset. The decay rate is faster in the beginning and then becomes slower. The  $\tau$  value increases from several seconds to 50 seconds with the training pulse number from 10 to 120, revealing a declining forgetting rate from  $\sim 57\%$  for  $N = 10$  to  $\sim 5\%$  for  $N = 120$ . This confirms the transition from STP to LTP through repeated rehearsal and learning.

The STDP rule has been mimicked in TiN/HfO<sub>x</sub>/AlO<sub>x</sub>/Pt memristor, as indicated in **Figure 5**. The schematic of another training pulse signal with various amplitudes is shown in **Figure 5a**, different from the pulse design in **Figure 2**. A set of pulses (1 V, -0.5 V, -0.45 V, -0.4 V, -0.35 V, -0.3 V, -0.25 V)/(0.5 V, -1 V, -0.9 V, -0.8 V, -0.7 V, -0.6 V, -0.5 V) were used as pre-synaptic/post-synaptic stimulation signals, respectively. Some different pulse signals designed at various spike timings ( $\Delta t$ ) are designed and illustrated in **Figure 5b**. When the shortest  $\Delta t$  (10 ms) is inserted to the device, the largest  $\Delta W$  of 50% for potentiation and -80% for depression are realized.

The memristive mechanism of asymmetric TiN/HfO<sub>x</sub>/AlO<sub>x</sub>/Pt memristor has been deeply investigated with the aid of x-ray photoelectron spectroscopy (XPS) depth analyses, which will be discussed in the following Section 2.3.

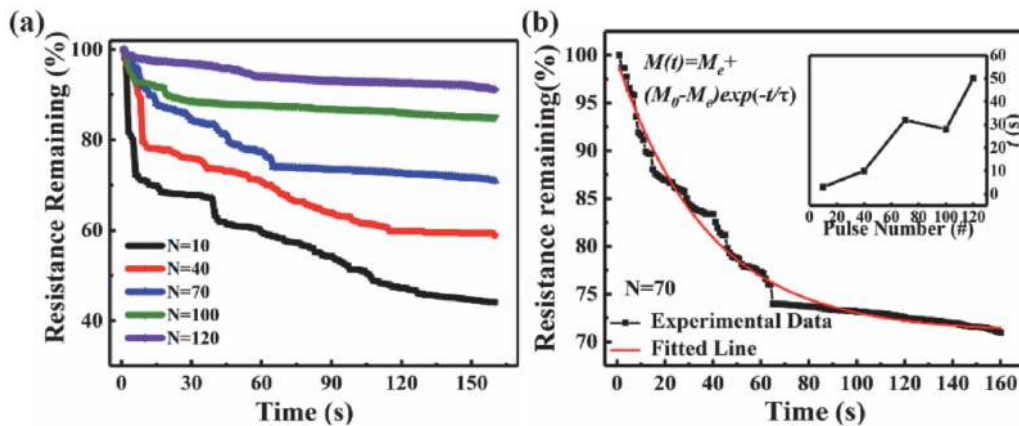


**Figure 4.** Repeated stimulation induced STP to LTP transition. (a) Resistance remaining decay curve recorded after 10, 40, 70, 100, 120 identical pulses (1.6 V, 10 ms). A 0.1 V voltage was used to read the device current. (b) Resistance remaining decay curve recorded after 70 identical pulses and the fitted curve according to Eq. (1). The inset plots the dependence of relaxation time  $\tau$  on the pulse number.  $\tau$  is obtained by the fitting curve [17].

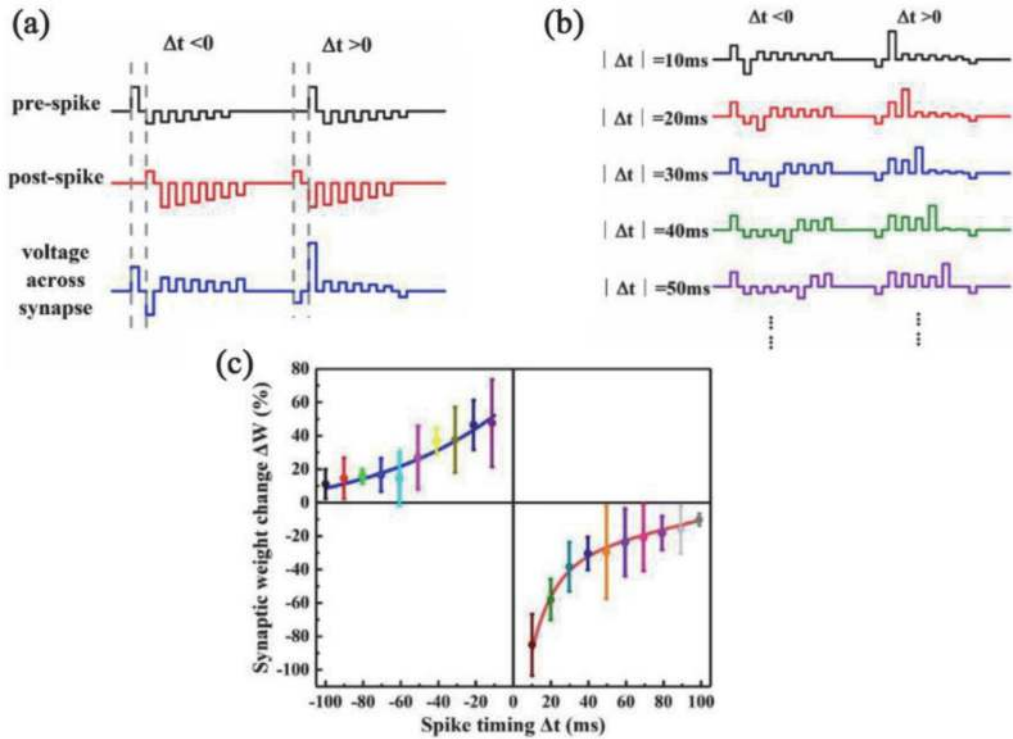


**Figure 5.** (a) Training pulse signal with different amplitudes design schematic loaded on the Pt/AlO<sub>x</sub>/HfO<sub>x</sub>/TiN memristor (assuming  $\Delta t = 10$  ms). Each pulse width and pulse interval are 10 ms, respectively. (b) Some different pulse signals designed at various spike timings ( $\Delta t$ ). (c) STDP-like curves. The relative change of the memristor synaptic weight ( $\Delta W$ ) versus the relative spike timing ( $\Delta t$ ) [17].

### 2.2.3 TiN/HfO<sub>x</sub>/HfO<sub>2</sub>/Pt inorganic memristor

In the previous work on Pt/HfO<sub>x</sub>/ZnO<sub>x</sub>/TiN and TiN/HfO<sub>x</sub>/AlO<sub>x</sub>/Pt memristors, the asymmetric memristive functional layers of A and B are different materials. Next, we will focus on Pt/HfO<sub>2</sub>/HfO<sub>x</sub>/TiN bilayer-structured memristor, as illustrated in **Figure 6a**. 4 nm-thick non-stoichiometric HfO<sub>x</sub> films were prepared by

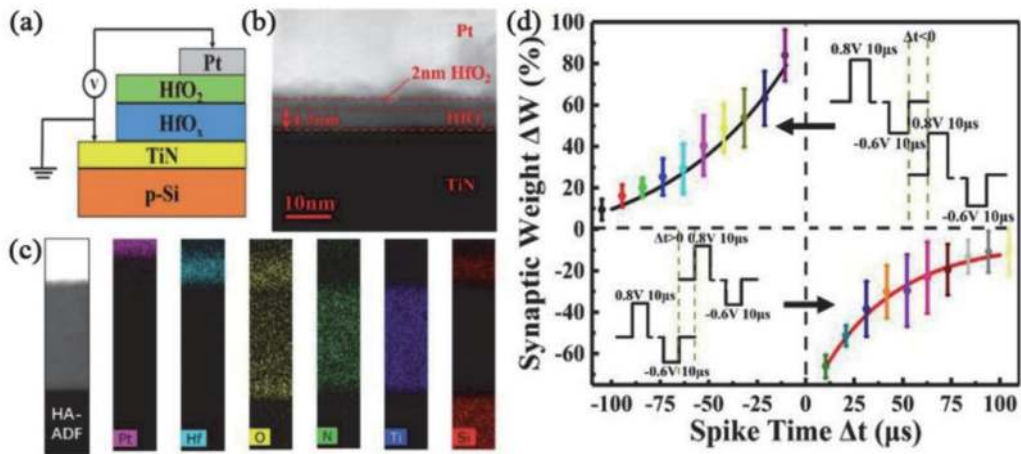


**Figure 6.** (a) Schematic of the Pt/HfO<sub>2</sub>/HfO<sub>x</sub>/TiN memristor. (b) Cross sectional HAADF-STEM image of the device. (c) EDS elemental mapping of Pt, Hf, O, N, Ti and Si. (d) STDP-like curves. The different synaptic weights ( $\Delta W$ ) versus the different spike times ( $\Delta t$ ). The inset shows a pair of pre-synaptic and post-synaptic spikes, and the spike pair is designed to implement STDP [20].

PEALD using the H<sub>2</sub> plasma and 2 nm-thick stoichiometric HfO<sub>2</sub> films by TALD using the H<sub>2</sub>O precursor, in basically consistent with the measured result by the cross-sectional high angle annular dark field (HAADF)-scanning transmission microscopy (STEM) in **Figure 6b**. The energy dispersive x-ray spectroscopy (EDS) elemental mapping images of Pt/HfO<sub>2</sub>/HfO<sub>x</sub>/TiN are shown in **Figure 6c**, revealing the stacking structure. In addition, XPS composition analyses show that the atomic ratio of Hf:O in the HfO<sub>2</sub> and HfO<sub>x</sub> layers is 1:2.04 and 1:1.84, respectively, indicating that stoichiometric HfO<sub>2</sub> and nonstoichiometric HfO<sub>x</sub> bilayer-structured memristors have been obtained [20]. Hence A and B herein represent HfO<sub>2</sub> and HfO<sub>x</sub> with various oxygen contents, respectively. This device unit based on TiN/HfO<sub>x</sub>/HfO<sub>2</sub>/Pt memristor can also simulate the biological synapse learning rule of STDP, as indicated in **Figure 6d**. When the shortest spike timing of 10 ms is applied to the memristor device, the pulse train responses give rise to the largest  $\Delta W$  value of 83% for potentiation and -65% for depression, respectively [20]. These  $\Delta W$  values for STDP are similar for Pt/HfO<sub>x</sub>/ZnO<sub>x</sub>/TiN, TiN/HfO<sub>x</sub>/AlO<sub>x</sub>/Pt and TiN/HfO<sub>x</sub>/HfO<sub>2</sub>/Pt memristors.

The paired-pulse facilitation (PPF) is a phenomenon wherein the post-synaptic response induced by the spike increases when the time interval of the two spikes is very close [20]. PPF index can be defined as follows:

$$\text{PPF} = (G_2 - G_1)/G_1 - 100\% = C_1 \cdot \exp(-\Delta t/\tau_1) + C_2 \cdot \exp(-\Delta t/\tau_2) \quad (3)$$

$G_1$  and  $G_2$  are the conductance values after the first and the second pulse, respectively. The time constants of  $\tau_1$  and  $\tau_2$  can be assigned to the fast and slow decaying terms, respectively.

Evidently Pt/HfO<sub>2</sub>/HfO<sub>x</sub>/TiN memristor displays the marked dependence of synaptic weight on pulse interval  $\Delta t$  by applying the pulse of -1.5 V and 2.5 V, respectively, as seen in **Figure 7a** and **b**. For shortest  $\Delta t$  of 400 ns, the PPF index increases to 135% under positive pulse and becomes -62% under negative pulse. For the negative pulse signals, the calculated  $\tau_1$  and  $\tau_2$  values are 357 ns and 2.47 ms, respectively; for the positive pulses,  $\tau_1$  and  $\tau_2$  are 1.48 ms and 6.79 ms, respectively. When the  $\Delta t$  decreases, the memory effect will be improved, which is ascribed to the fact that the smaller  $\Delta t$  between pulses produces less oxygen vacancies to drift back with more effective accumulation of the oxygen vacancies.

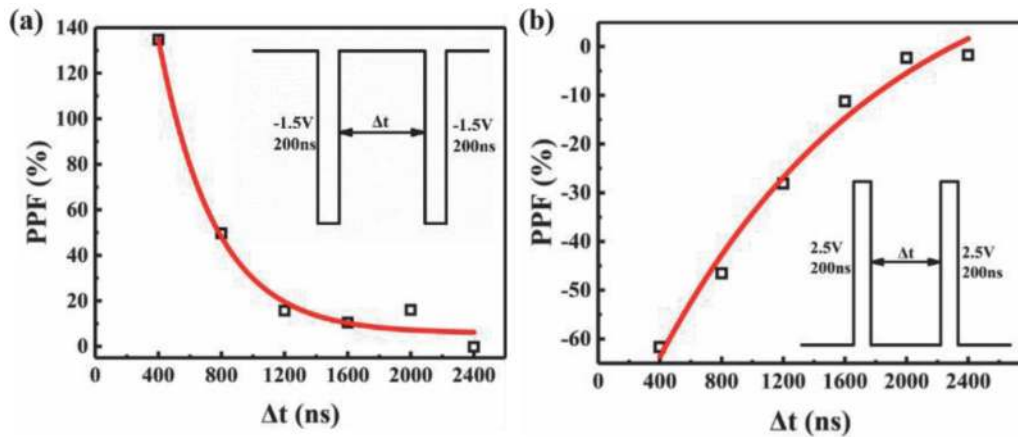


**Figure 7.** PPF index as the function of the time interval ( $\Delta t$ ) of the Pt/HfO<sub>2</sub>/HfO<sub>x</sub>/TiN memristor under negative voltage pulse (a) and positive voltage pulse (b). Black points represent the measurement data, and the red lines represent the fitting data by using Eq. (3). The insets in (a) and (b) record the applied pulse waveforms [20].



Pt/HfO<sub>2</sub>/HfO<sub>x</sub>/TiN also mimics a classical conditioning under different pulse stimuli, as illustrated in **Figure 8**. In the famous experiment [21], a dog salivates (unconditioned response, UR) when watching the food (unconditioned stimulus, US) (**Figure 8a**), when it does not salivate (conditioned response, CR) on hearing the ring (conditioned stimulus, CS) alone (**Figure 8b**). Nonetheless, after some rehearsals, *i.e.* feeding the dog when ringing the bell (**Figure 8c**), the dog salivates even in only hearing the ring (**Figure 8d**). This elucidates that the dog has correlated the food with the ring. Furthermore, when taking away the food, the correlation between the food and ring gradually reduces and even disappears under only the conditioned stimuli (**Figure 8e**). The whole procedure can be emulated in the Pt/HfO<sub>2</sub>/HfO<sub>x</sub>/TiN by using +4 V and -1.3 V stimuli with a single pulse duration of 5 ms.

Before rehearsing, the memristor has a low resistance state of 5 kΩ. The +4 V stimulus (US) causes a high resistance state of 3 MΩ (UR) (**Figure 8f**), when the -1.3 V stimulus (CS) only results in a low resistance state of 5 kΩ before training (**Figure 8g**). In Pavlov's experiments, the food and the ring exist simultaneously to reinforce the correlation between US and CS. In our experiments, the +2.7 V stimulus was exerted to the memristor, the same as the simultaneous stimuli of -1.3 V and +4 V pulse signals. When two rehearsing sequences with +2.7 V pulse, the device becomes the high resistance output of 2 MΩ (CR) (**Figure 8h**). When removing the +4 V signal, the memristor continues to keep in a high resistance state under a series of -1.3 V stimuli alone and then returns to a low resistance state (**Figure 8i**), implying the setup and vanish of the classical conditional reflex.

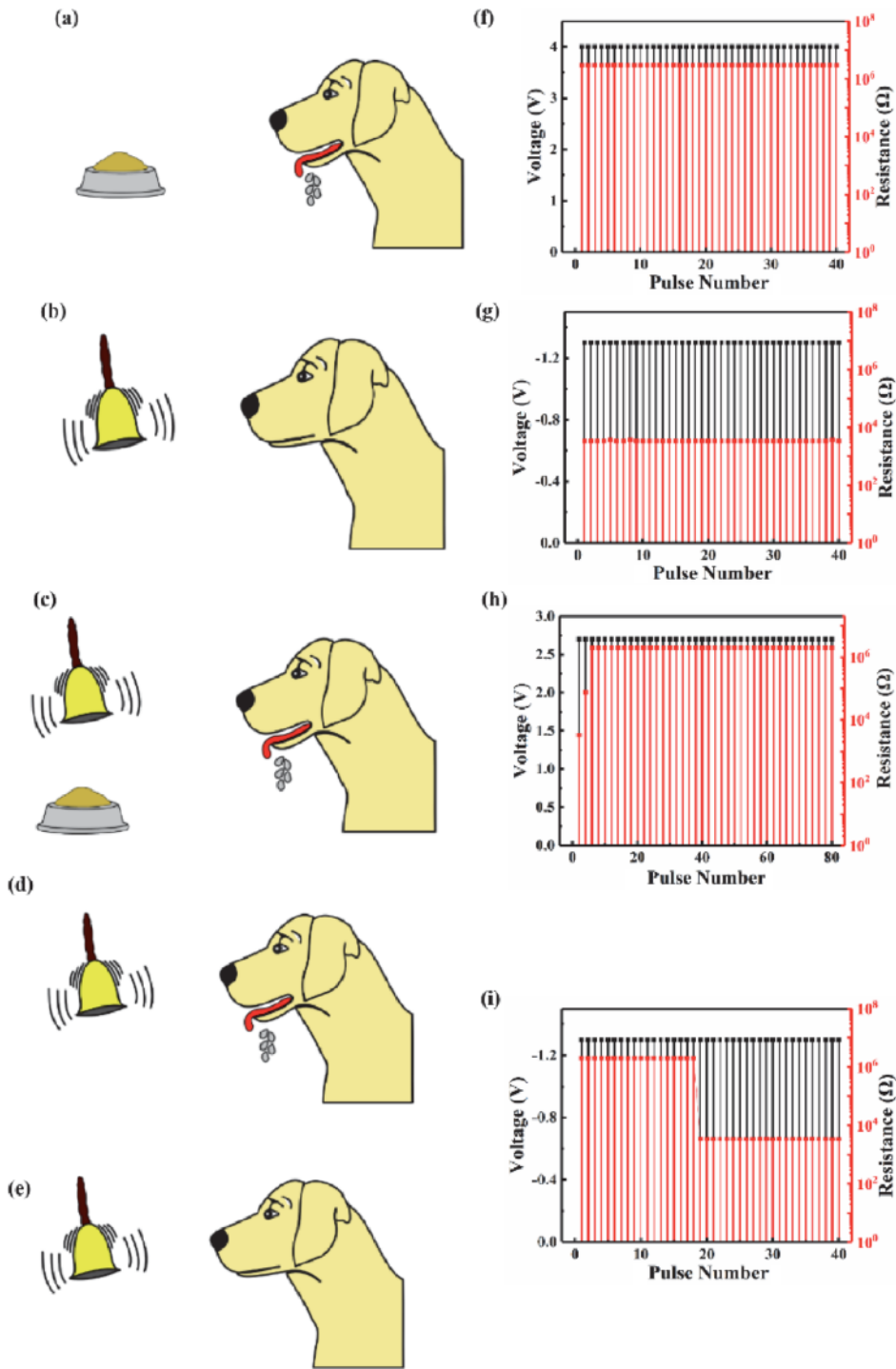
The energy consumption is one important indicator for a practical electronic synaptic device in neuromorphic network. Pt/HfO<sub>2</sub>/HfO<sub>x</sub>/TiN memristor can be set in less than 100 ns and reset in less than 10 ns, indicating the rapid switching speed, as recorded in **Figure 9a**.

The current response curves versus the time after the applied programming signal during the set or reset operation are plotted in **Figure 9b** and **c**, respectively. The current rises after a waiting time of about 260 ns when a -2 V/1 ms stimulus is applied, indicating the beginning of the set process (**Figure 9b**). The memristor resistance decreases from the initial high resistance state (~1 MΩ) to low resistance state (~800 Ω). Similarly, the current reduces after a waiting time of about 70 ns when a +3 V/1 ms signal is exerted, showing the occurrence of the reset process. The energy consumption per operation can be calculated to be 520 pJ for the set process and 1.05 nJ for the reset process by considering the pulse waveforms (time, response current, and pulse voltage), corresponding to the maximum energy consumption in one set or reset operation, as the memristor has been set in the lowest resistance state with the highest response current. Nevertheless, the actual operation of the electronic synapse is generally in the mediate resistance states (~80 kΩ). The response current of the memristor is inversely proportional to the resistance value of the synaptic device with a first-order approximation. So, the evaluated actual energy consumption per operation will decline in the range of around ten picojoules.

Finally, the impact of oxygen vacancy concentration in non-stoichiometric HfO<sub>x</sub> layers on resistive switching properties of Pt/HfO<sub>2</sub>/HfO<sub>x</sub>/TiN bilayer ultrathin memristor has been investigated. The memristor with 12.1% oxygen vacancy concentration in the HfO<sub>x</sub> layer exhibits comprehensively better performances such as the optimal pulse energy consumption, reset switching speed, and DC endurance and retention characteristics [20].

#### 2.2.4 TaN/Ti-MA/TiO<sub>2</sub>/Pt organic: inorganic hybrid memristor

As mentioned above, we mainly elucidated the bio-synaptic functions of three asymmetric inorganic bilayer-structured ultrathin memristors. In this part,


**Figure 8.**

Emulation of the acquisition and extinction of classical conditioning demonstrated by Pavlov's dog experiment. (a) The dog salivates while watching the food (US  $\rightarrow$  salivating UR). (b) The dog does not salivate upon hearing the ringing alone (CS  $\rightarrow$  no salivating). (c) In the training process, the food and ringing together stimulates the dog, and the dog salivates (US + CS  $\rightarrow$  salivating). (d) After sufficient training, classical conditioning is formed and the dog salivates upon hearing the ringing alone (CS  $\rightarrow$  salivating, CR). (e) Extinction of classical conditioning after removing the food for some time. (f) Positive +4 V pulse (US) can lead to a high resistance output, similar to the UR in (a). (g) The negative -1.3 V pulse (CS) cannot lead to the high resistance output before training, similar to the CS in (b). (h) After applying several training sequences of +2.7 V pulse voltage, equal to the simultaneous stimuli of -1.3 V and +4 V pulses, the device reaches a high resistance state of 2 M $\Omega$  (CR), analogous to the phenomenon in (c). (i) After only applying some -1.3 V pulse alone, the memristor remains in a high resistance state, similar to CR in (d). Then it returns to the low resistance state, consistent with the extinction of classical conditioning in (e) [20].

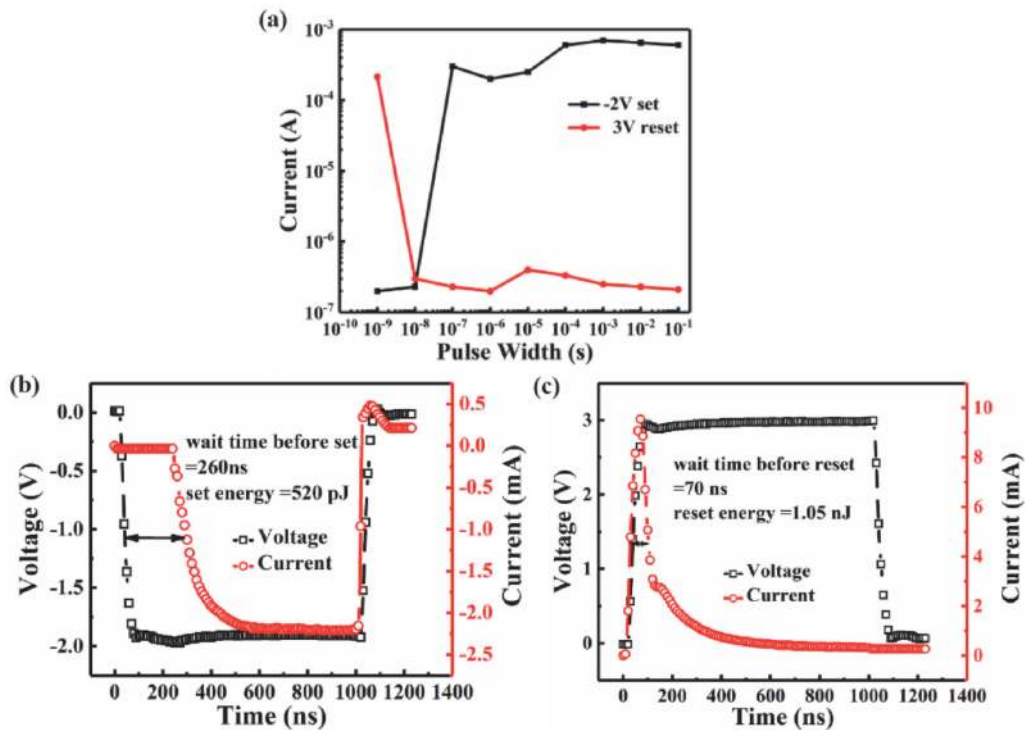


**Figure 9.** (a) Switching speed test of the synaptic device. The voltage for the set and reset operation in the memristor is about  $-2$  V and  $+3$  V, respectively. The device can be switched in less than  $100$  ns for a set operation and less than  $10$  ns for a reset operation. (b) Transient current response on the applied voltage pulse for a set operation from the high resistance state to the low resistance state. The set pulse amplitude, width, rising time, and falling time are set to be  $-2$  V,  $1000$  ns,  $20$  ns, and  $20$  ns, respectively. (c) Transient current response on the applied voltage pulse for a reset operation from the low resistance state to the high resistance state. The reset pulse amplitude, width, rising time, and falling time are set to be  $3$  V,  $1000$  ns,  $20$  ns, and  $20$  ns, respectively [20].

organic–inorganic hybrid bilayer memristors of TaN/Ti-MA/TiO<sub>2</sub>/Pt were prepared by low temperature MLD/ALD at  $160^{\circ}\text{C}$ . The synaptic plasticity has been explored deeply. Some superb synaptic functions, such as nonlinear transmission characteristics, STP/LTP, PPF, and STDP have been achieved in the hybrid memristors [22].

First the narrow-scan XPS and Fourier transform infrared (FTIR) spectroscopy were used to detect the chemical composition and organic group of Ti-based maleic acid (Ti-MA) hybrid film, as shown in **Figure 10a–d**. The C 1s XPS peaks at  $284.6$  eV and  $288.4$  eV (**Figure 10a**) result from the C-C (backbone chain carbon) bond and the O-C=O bond from carboxyl, respectively, suggesting the occurrence of organic component in Ti-MA films. The doublet at  $458.7$  eV and  $464.5$  eV with the spin orbit splitting energy of  $5.8$  eV can be assigned to the Ti  $2p_{1/2}$  and Ti  $2p_{3/2}$  ones from the Ti-O bond of TiO<sub>2</sub> [13, 23] (**Figure 10b**, which indicates the inorganic component in hybrid films. Moreover, the O 1s spectrum can be deconvoluted into two peaks at  $530.0$  eV and  $531.6$  eV, corresponding the O-Ti and O-C bonds, respectively (**Figure 10c**). The FTIR spectrum of Ti-MA hybrid film (**Figure 10d**) displays the asymmetric and symmetric stretch of carboxylate groups at  $1575\text{ cm}^{-1}$  and  $1447\text{ cm}^{-1}$ . The splitting of  $128\text{ cm}^{-1}$  indicates the bidentate bond mode between the Ti ion and carboxyl. As a result, Ti-MA inorganic–organic hybrid films have been fabricated successfully.

The resistive switching characteristics of the hybrid bilayer memristor of TaN/Ti-MA/TiO<sub>2</sub>/Pt have been examined for 100 times, as seen in **Figure 11a**. The typical bipolar resistive switching behavior has been confirmed with narrow distribution of set voltage of  $-1.6 \pm 0.2$  V (red line) or reset voltage of  $1 \pm 0.1$  V

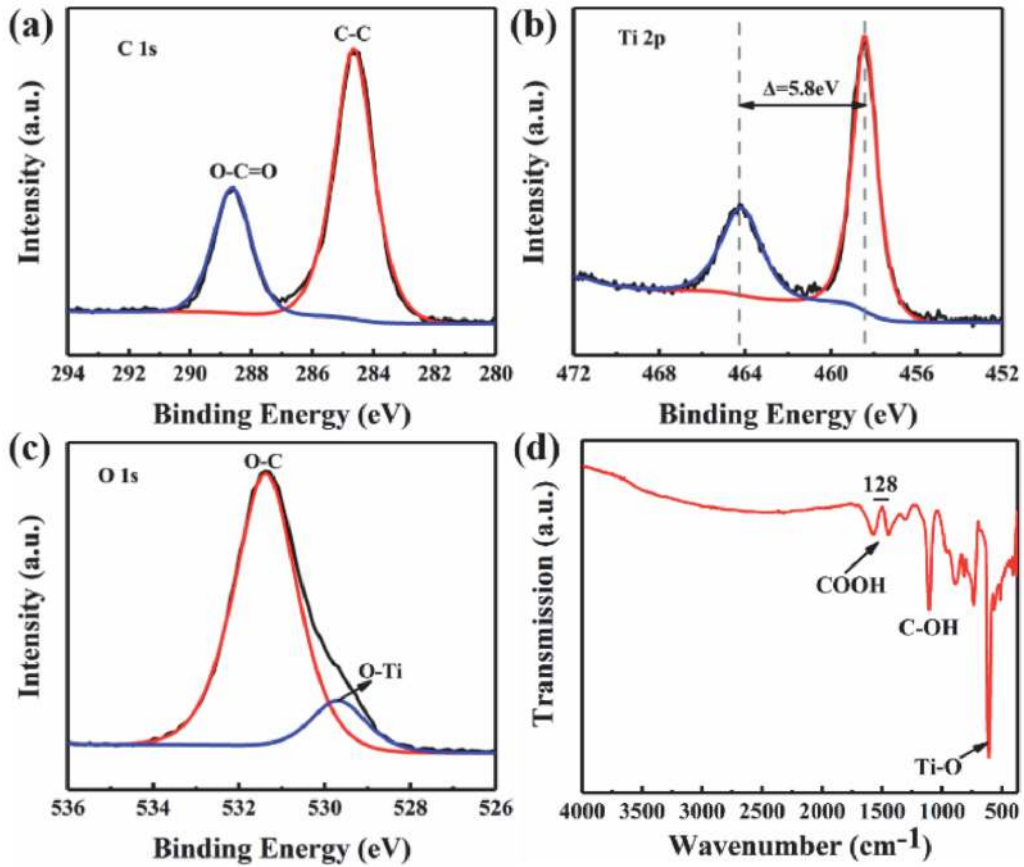


**Figure 10.** Narrow-scan XPS spectra of (a) C 1s, (b) Ti 2p and (c) O 1s and (d) FTIR spectrum from the Ti-MA hybrid films on Si [22].

(black line). The double-logarithmic  $I$ - $V$  curves and linear fits to the set process are shown in **Figure 11b**. At the low voltage stage, the  $I$ - $V$  is dominated by the Ohm's law with the approximately linear relationship (region 1,  $R^2 = 0.9996$ ). When the voltage increases, the current is dependent of near square of the voltage, obeying the Child conductive law (region 2,  $R^2 = 0.9995$ ). At critical voltage of around 1.2 V, the current is proportional to the  $n$ th power of the voltage with a sharp current rise

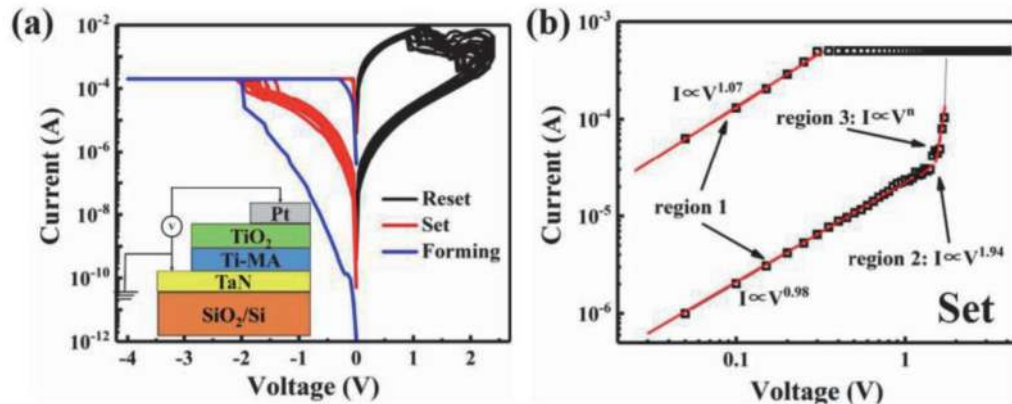


**Figure 11.** (a)  $I$ - $V$  curve of the TaN/Ti-MA/TiO<sub>2</sub>/Pt hybrid memristor for 100 times DC ramp voltages tests. Bottom inset is the schematic of the memristor. (b) Double-logarithmic  $I$ - $V$  curves and linear fits to the set process [22].



(region 3,  $R^2 = 0.9904$ ). All these prove the space charge limited current (SCLC) model in hybrid bilayer memristor [24], revealing the filament model of oxygen vacancy migration.

The PPF and STDP functions have also been characterized in hybrid memristor, as shown in **Figures 12** and **13**, respectively. A pair of pulses ( $-1$  V, 400 ns) with different  $\Delta t$  were applied to the hybrid memristor (**Figure 12a**). The measured data can be well fit exponentially (**Figure 12b**). The PPF index has reached to 361% with the 400 ns pulse interval in hybrid memristor. When the pulse interval increases to 2400 ns, the PPF index dramatically tends to 3% [22]. Compared to inorganic bilayer memristor, the organic–inorganic hybrid bilayer device has much larger PPF index in the same pulse interval of 400 ns.

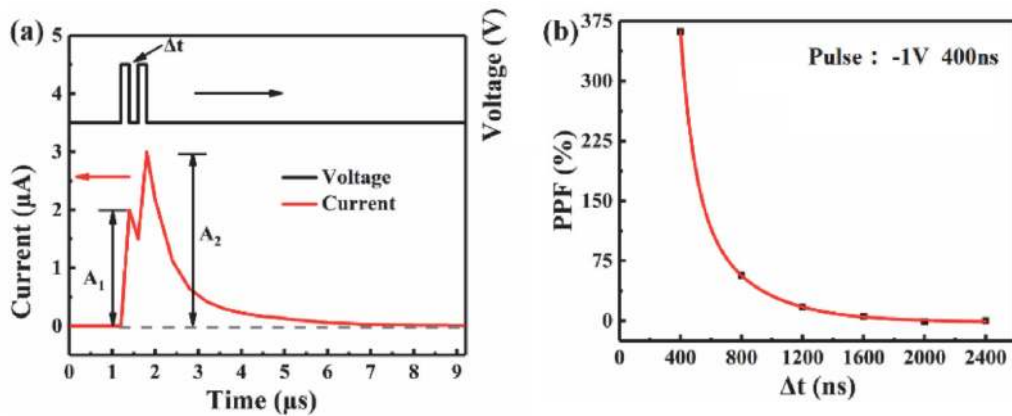


**Figure 12.** (a) PPF function in memristors generated by two pulse spikes and the real-time response current. (b) PPF curves with different pulse interval time [22].

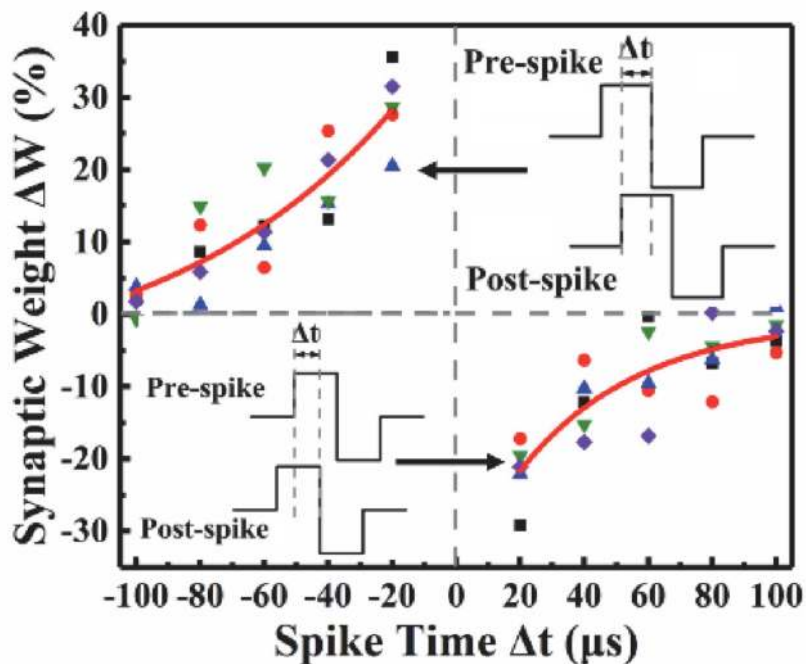


**Figure 13.** STDP curves obtained in hybrid memristor. The spot is the measured data and the red line is the fitting results. The insets are the spike pulse signals designed by a pair of 0.8 V and  $-0.8$  V pulses with pulse width of 120  $\mu\text{s}$  [22].

The STDP rule was emulated in hybrid memristor by using a pair of 0.8 V and  $-0.8$  V pulses with  $120 \mu\text{s}$  pulse width. The  $\Delta W$  has a strong time correlation with maximum 35% increment at the  $\Delta t$  of  $-20 \mu\text{s}$  and  $-20\%$  reduction at the  $\Delta t$  of  $20 \mu\text{s}$ . These values are relatively smaller than the  $\Delta W$  maximum value of 60–90% of inorganic memristors. Finally, the  $\Delta W$  in hybrid device obeys the exponential association with the  $\Delta t$ , namely

$$\Delta W = A \exp(-\Delta t/\tau) \quad (4)$$

The measured data can be fitted well.

In addition, the conditioned reflex has been mimicked in hybrid film memristor, similar to the results of Pt/HfO<sub>2</sub>/HfO<sub>x</sub>/TiN memristor in **Figure 8**.

By comparison with inorganic bilayer memristors, it can be found that the organic–inorganic hybrid bilayer memristor has similar bio-synaptic functions with comparable switching speed and energy consumption. Moreover organic–inorganic hybrid materials may possess both the advantages of organic and inorganic components with excellent flexibility and tunability. Inorganic compounds have better electrical characteristics and thermal stability. Organic compounds own various functional groups, larger stretchability and low processing temperature. By means of the synergetic and complementary effects between organic and inorganic components, the comprehensive properties of hybrid memristive materials could be expected for significant improvement. The hybrid bilayer ultrathin memristor derived by low temperature MLD/ALD is one competitive candidate for flexible neuroscience applications.

### 2.3 Memristive mechanism

In Section 2.2, we focused on the electrical Performance and synaptic functions of several bilayer ultrathin memristors. In this section, the asymmetric memristive mechanism of the bilayer-structured memristors on TiN or TaN will be studied carefully. Taking Pt/AlO<sub>x</sub>/HfO<sub>x</sub>/TiN memristor as an example, the XPS depth profiles of asymmetric bilayer device units were obtained under various resistance states of the initial state, low resistance state (LRS), high resistance state (HRS), and medium resistance state [17]. XPS is a powerful surface analytical tool to determine the chemical valence and the oxygen vacancy contents in multilayer-structured metal oxide thin films [23, 25].

**Figure 14a–d** records the high-resolution Al 2p, Hf 4f and O 1 s peaks in AlO<sub>x</sub> and HfO<sub>x</sub> layers for as-deposited Pt/AlO<sub>x</sub>/HfO<sub>x</sub>/TiN in the initial state. The Hf 4f spectra from the HfO<sub>x</sub> layer can be deconvoluted into four peaks (**Figure 14b**). The stronger peaks at  $\sim 16.7$  eV and 18.6 eV originate from the Hf<sup>4+</sup> in the HfO<sub>x</sub> layer, whereas the weaker ones with slightly lower energies of 15.6 eV and 17.9 eV come from the Hf<sup>(4-x)+</sup> in the low valence Hf sub-oxide. The content percentage of two Hf valence states in the HfO<sub>x</sub> layer can be roughly evaluated by calculating the area proportion of each peak, as shown in the inset of **Figure 14b** [26–28]. The percentage of Hf<sup>4+</sup> and Hf<sup>(4-x)+</sup> in the HfO<sub>x</sub> layer is around 89.7% and 9.4%, respectively. A similar analysis can be also carried out for the Al 2p spectra from AlO<sub>x</sub> layer (**Figure 14a**). Meanwhile the O 1 s spectra from the AlO<sub>x</sub> and HfO<sub>x</sub> layers can also be deconvoluted into two peaks. The stronger peaks at around 531.5 and 531.0 eV result from Al–O and Hf–O bonding in the AlO<sub>x</sub> and HfO<sub>x</sub> layers, respectively, whereas the weaker ones with a slightly higher energy of 532.1 eV in the O 1 s spectra are ascribed to the oxygen vacancies in the AlO<sub>x</sub> and HfO<sub>x</sub> layers according to the literature reports [26–29]. The calculated percentage of oxygen vacancies in the AlO<sub>x</sub> and HfO<sub>x</sub> layers is around 0.7% and 8.1%, respectively (**Figure 14c and d**).

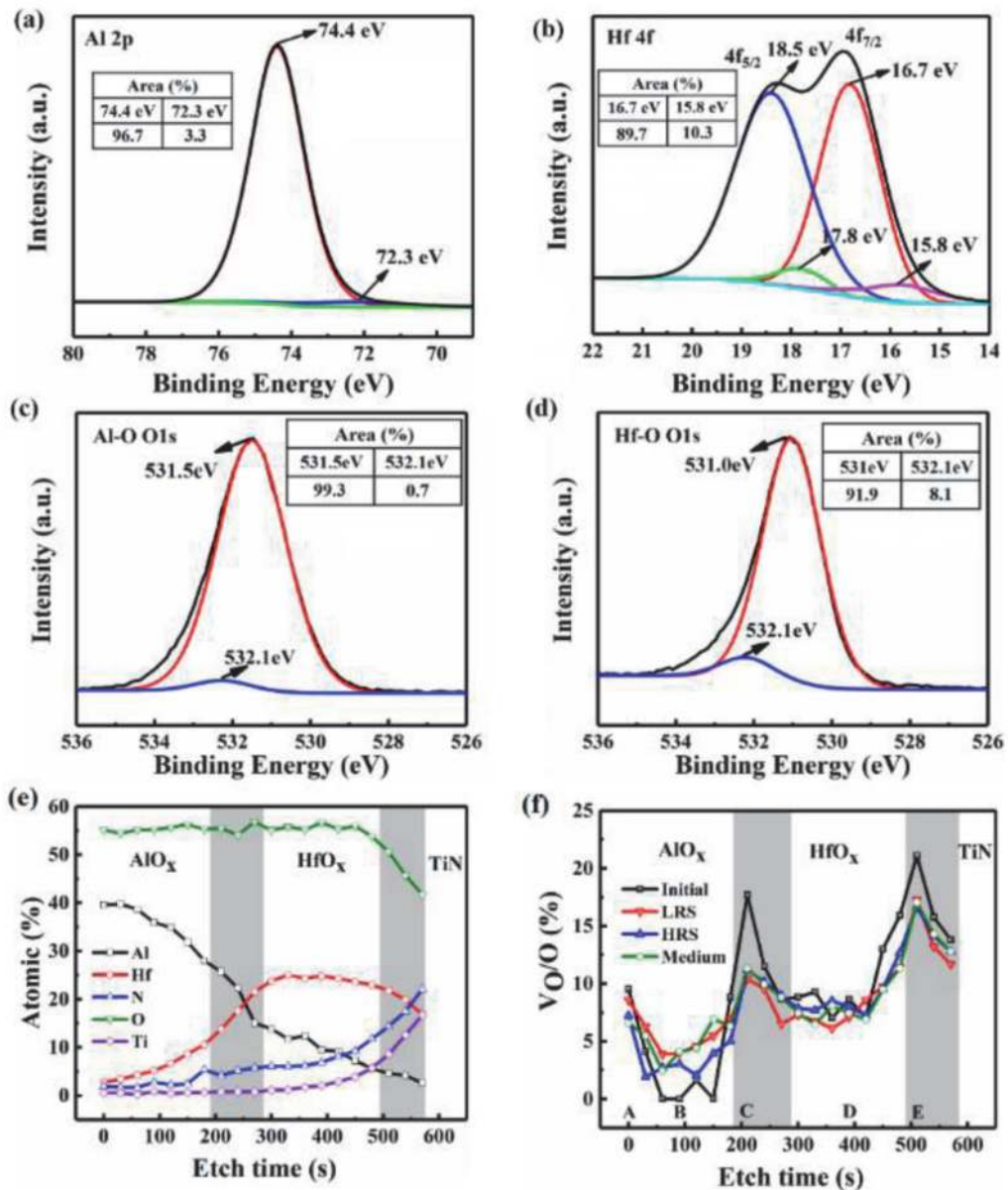


**Figure 14.** Narrow-scan (a) Al 2p, (b) Hf 4f and O 1s peaks of (c) AlO<sub>x</sub> and (d) HfO<sub>x</sub> in as-prepared Pt/AlO<sub>x</sub>/HfO<sub>x</sub>/TiN in the initial state. (e) XPS depth profile of Pt/AlO<sub>x</sub>/HfO<sub>x</sub>/TiN in the initial state. (f) The depth distribution of the average oxygen vacancy concentration in the initial state, LRS, HRS, and medium resistance state after 40 pulses (1.5 V, 0.5 ms). The gray region in figure (e) and (f) is the interfacial layer [17].

Significantly, the oxygen vacancy content in the HfO<sub>x</sub> layer is much higher than that in the AlO<sub>x</sub> layer.

The XPS depth data of Pt/AlO<sub>x</sub>/HfO<sub>x</sub>/TiN memristor by Ar ion etching under various resistance states may provide some valuable information on the valence states and defects of metal oxide layers [24], for the initial state sample recorded in **Figure 14e**. The AlO<sub>x</sub>/HfO<sub>x</sub> bilayer structure could be recognized with an evident interfacial diffusion between AlO<sub>x</sub>/HfO<sub>x</sub> and HfO<sub>x</sub>/TiN (gray region). The depth distribution of the average oxygen vacancy concentration in the asymmetric Pt/AlO<sub>x</sub>/HfO<sub>x</sub>/TiN memristors under various resistance states of the initial state, LRS, HRS, and medium resistance state is illustrated in **Figure 14f**. **Table 3** lists the average oxygen vacancy concentration values of Pt/AlO<sub>x</sub>/HfO<sub>x</sub>/TiN for four resistance states at different positions of A, B, C, D, and E, corresponding to an etch time

of 0 s, 90 s, 210 s, 390 s, and 510 s. Herein A, B, C, D, and E locate in the interface of the Pt/ $\text{AlO}_x$ ,  $\text{AlO}_x$  layer, the interface of the  $\text{AlO}_x/\text{HfO}_x$ ,  $\text{HfO}_x$  layer, and the interface of  $\text{HfO}_x/\text{TiN}$ , respectively. The oxygen vacancy distribution is inhomogeneous in the Pt/ $\text{AlO}_x/\text{HfO}_x/\text{TiN}$  memristor, and the oxygen vacancy concentration of the interfaces between  $\text{AlO}_x/\text{Pt}$  (A),  $\text{AlO}_x/\text{HfO}_x$  (C),  $\text{HfO}_x/\text{TiN}$  (E) is markedly higher than that of the adjacent  $\text{AlO}_x$  (B) and  $\text{HfO}_x$  (D) layers. Furthermore, the oxygen vacancy concentration in  $\text{HfO}_x$  (D) is much higher than that in  $\text{AlO}_x$  (B) layer.

In general, the resistive switching mechanism of metal oxide memristors is related to the connection and rupture of conductive filaments of oxygen vacancies. But the simple increase of oxygen vacancy concentration is not always effective. The non-uniform distribution of oxygen vacancies in memristors is the critical factor affecting the resistive switching behavior of memristive devices [30].

Based on the oxygen vacancy concentration and distribution in the Pt/ $\text{AlO}_x/\text{HfO}_x/\text{TiN}$  memristors under various resistance states in **Figure 14f**, we proposed a memristive mechanism of an asymmetric bilayer metal oxide synaptic device to explain synaptic plasticity, as illustrated in **Figure 15**.

There are much more random oxygen vacancies in the  $\text{HfO}_x$  layer than in the  $\text{AlO}_x$  layer for as-deposited Pt/ $\text{AlO}_x/\text{HfO}_x/\text{TiN}$  device. Meanwhile, the oxygen vacancy concentration in the interfaces of  $\text{AlO}_x/\text{HfO}_x$  and  $\text{HfO}_x/\text{TiN}$  is evidently higher than the  $\text{HfO}_x$  layer (**Figure 15a**). During the forming process, the disorderly distributed oxygen vacancies in the bilayer oxide layers and interfacial layers form conductive filaments under the external electrical field, similar to the soft breakdown of the capacitor. So the connection and disconnection of the conductive filaments lead to resistive switching. When inserting a  $-3$  V forming voltage, the device turns from the initial state to LRS with suddenly resistance drop from  $10$  M $\Omega$  to  $600$   $\Omega$ , suggesting that the oxygen vacancies with positive charges ( $\text{V}_\text{O}^{2+}$ ) in the  $\text{AlO}_x/\text{HfO}_x$  interface,  $\text{HfO}_x$  layer, and  $\text{HfO}_x/\text{TiN}$  interface move to the  $\text{AlO}_x$  layer and  $\text{AlO}_x/\text{Pt}$  interface. Simultaneously, the oxygen vacancy concentration gradient help to the migration of the oxygen vacancies, forming localized conductive filaments of oxygen vacancies in the bilayer structured  $\text{AlO}_x/\text{HfO}_x$  device (**Figure 15b**).

After applying the  $+2.5$  V reset voltage to the LRS device, the memristor transfers from LRS ( $600$   $\Omega$ ) to HRS ( $1$  M $\Omega$ ) (**Figure 15c**). During the reset process, the oxygen vacancies migrate from the  $\text{AlO}_x/\text{Pt}$  interface and  $\text{AlO}_x$  layer to the  $\text{AlO}_x/\text{HfO}_x$  interface and  $\text{HfO}_x$  layer, leading to the rupture of oxygen vacancy conductive filaments in the  $\text{AlO}_x$  layer. Besides, considering the thermophoresis/diffusion-driven oxygen migration [31, 32], the middle position of the conductive filament in the  $\text{AlO}_x$  layer first breaks up, causing a spatial gap, as indicated by the red arrow in **Figure 15c**. *electron* tunneling happens through the physical gap with the enhanced resistance. During the reset process, the oxygen vacancy concentration declines at the  $\text{AlO}_x/\text{Pt}$  interface and  $\text{AlO}_x$  layer and rises at the  $\text{AlO}_x/\text{HfO}_x$  interface and  $\text{HfO}_x$ .

Oxygen vacancy concentration	A	B	C	D	E
Position	Pt/ $\text{AlO}_x$	$\text{AlO}_x$	$\text{AlO}_x/\text{HfO}_x$	$\text{HfO}_x$	$\text{HfO}_x/\text{TiN}$
Initial	9.5%	0.7%	17.7%	8.7%	21.1%
LRS	8.8%	4.1%	10.4%	7.1%	17.3%
HRS	7.2%	3.0%	11.2%	8.0%	16.7%
Medium	6.6%	4.0%	11.3%	7.5%	17.0%

**Table 3.**

Average oxygen vacancy concentration of Pt/ $\text{AlO}_x/\text{HfO}_x/\text{TiN}$  in various positions for different resistance states [17].



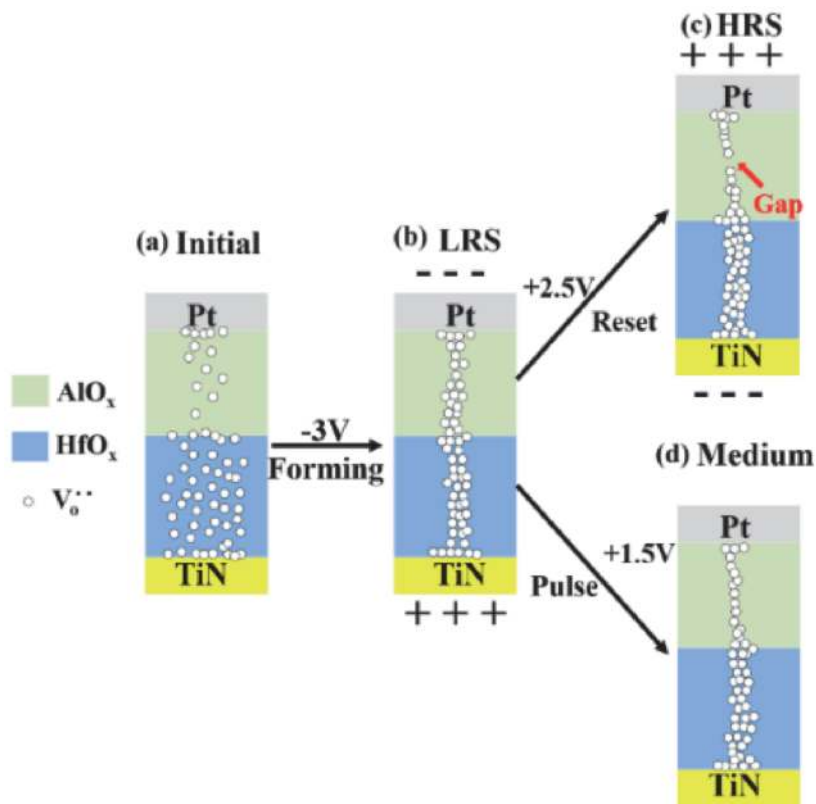


**Figure 15.** Model of the formation and rupture of a conductive filament consisting of oxygen vacancies. After  $-3$  V forming voltage, the device transfers from an initial resistance state (a) to a low resistance state (LRS) (b); after  $2.5$  V reset voltage, the device transfers from a low resistance state to a high resistance state (HRS) (c); after 40 continuous pulses ( $+1.5$  V,  $10$  ms), the device transfers from LRS to a medium resistance state (d) [17].

layer, as proved by the relative variation of oxygen vacancy concentrations in **Figure 14f** and **Table 3**.

Because the synapse device usually operates under pulse mode to get more intermediate resistance states, a continuous pulse experiment was exploited to alter the device from a LRS ( $600 \Omega$ ) to a medium resistance state ( $50 \text{ k}\Omega$ ) by imposing 40 pulses ( $+1.5$  V,  $10$  ms) (**Figure 15d**). The XPS result (**Figure 14f**) indicates that the oxygen vacancy concentration curve of medium resistance state devices lies approximately between HRS and LRS in the  $\text{AlO}_x$  layer and  $\text{HfO}_x$  layer. The difference in oxygen vacancy concentration at the interface layers of  $\text{AlO}_x/\text{HfO}_x$  and  $\text{HfO}_x/\text{TiN}$  among the medium resistance state, LRS, and HRS is slightly little. In consequence, during regular operations of synaptic memristors, the formation/rupture of nanoscale conductive filaments tend to appear in the low  $k$   $\text{AlO}_x$  layer with lower electric field intensity [33]. Furthermore, the device conductance can be modulated by the oxygen vacancy drift under pulse electric field, producing a change in the concentration and distribution of oxygen vacancies at the interface of the metal/oxide and the interior. In the LRS of  $600 \Omega$ , the conductive filament is thick with the conductance of  $22 G_0$ , corresponding to a wide conductive filament with classical metallic properties. After 40 pulse stimuli, a medium resistance state of  $50 \text{ k}\Omega$  is obtained with a conductance of  $0.26 G_0$ , where the conductive filament behaves as a quantum wire, producing a single-defect conducting path [31, 33, 34].

The oxygen vacancy migration/diffusion model can be used to explain the transition from STP to LTP in bilayer memristive device (**Figure 4a**). When imposing the  $+1.6$  V pulse, the oxygen vacancies move from the  $\text{AlO}_x$  layer to the  $\text{HfO}_x$  layer

with the reduced response current. When the voltage is removed, some oxygen vacancies may stay in a new steady position, however some oxygen vacancies may diffuse back to the old position owing to the gradient of oxygen concentration. This leads to the device conductance change with a reduced synaptic weight during the relaxation time. After applying repetitive pulse stimuli, the subsequent voltage forces the reversely diffused oxygen vacancies to move forward again so as to improve the migration efficiency until most oxygen vacancies attain new equilibrium positions. The remaining synaptic weight gradually increases with the increasing pulse number. This process is called repeated training and learning, corresponding to the transformation from STP to LTP [17].

The memristive mechanism from Pt/AlO<sub>x</sub>/HfO<sub>x</sub>/TiN device is also applicable to other bilayer-structured memristors such as Pt/HfO<sub>2</sub>/HfO<sub>x</sub>/TiN, Pt/TiO<sub>2</sub>/Ti-MA/TaN.

### 3. Conclusion

Our asymmetric bilayer-structured memristors fabricated by ALD/MLD and their main memristive features are summarized in **Table 4**, including set/reset voltage, ON/OFF ratio, and some important synaptic functions. Some similar work with asymmetric bilayer structure has also been listed in **Table 4** for comparison. It can be seen that all memristors with asymmetric bilayer structure exhibit better resistive switching performance. Our memristors have relatively thinner functional layers, relatively smaller ON/OFF ratio and emulate more artificial synaptic functions such as LTPo, LTD, the transition from STP to LTP, PPF, STDP, and conditional reflex (CR). The memristive mechanism of our bilayer-structured ultrathin device has been proposed to explain the synaptic plasticity based on oxygen vacancies migration/diffusion model. The non-uniform distribution of oxygen vacancies in asymmetric bilayer memristors plays the crucial role in affecting the linkage/rupture of conductive filaments.

In light of these promising results and the fabrication compatibility with semiconductor industry, the ALD/MLD-derived bi-layer ultrathin memristor devices have tremendous potential as billions of electronic synapses in next-generation artificial neural network and flexible electronics.

Device structure	Thickness (nm)	Set/reset voltage (V)	ON/OFF ratio	Synaptic functions	References
Pt/HfO <sub>2</sub> /ZnO/TiN	~10	-1.7/+1.4	~30	LTPo, LTD, STP/LTP, STDP	Our works
Pt/Al <sub>2</sub> O <sub>3</sub> /HfO <sub>2</sub> /TiN	~10	-1.4/ +1.3	~610	LTPo, LTD, STP/LTP, PPF, STDP	
Pt/HfO <sub>2</sub> /HfO <sub>x</sub> /TiN	~6	-1.6/+1.1	~954	LTPo, LTD, STP/LTP, PPF, STDP, CR	
Pt/TiO <sub>2</sub> /Ti-MA/TaN	~8	-1.5/+1	~230	LTPo, LTD, STP/LTP, PPF, STDP, CR	
Ni/SiN <sub>x</sub> /AlO <sub>y</sub> /TiN	~11.5	+4/-3.5	~500	LTPo, LTD, STDP	[35]
TiN/HfO <sub>2</sub> /Al <sub>2</sub> O <sub>3</sub> /Pt	~10	+1.4/-1.3	~10 <sup>5</sup>	STDP	[36]
W/AlO <sub>x</sub> /Al <sub>2</sub> O <sub>3</sub> /TiN	~10	+1.05/-1.25	~10 <sup>3</sup>	—	[37]
Ag/ZrO <sub>2</sub> /WS <sub>2</sub> /Pt	~100	+0.16/-0.06	>10 <sup>5</sup>	PPF, STDP	[38]

**Table 4.**

*Comparison of main memristive features of our ultrathin memristors fabricated by ALD/MLD and other asymmetric bilayer-structured memristors.*

## **Acknowledgements**

This work is supported by the Natural Science Foundation of China (52073142, 51721001) and Jiangsu Province (BK20201252). Mr. Chang Liu also acknowledges the support from the Nanjing University Innovation and Creative Program for PhD candidate (CXCY18-27).

## **Conflict of interest**

The authors declare no conflict of interest.


## **Author details**

Chang Liu, Lin Zhu, Lai-Guo Wang and Ai-Dong Li\*  
National Laboratory of Solid State Microstructures, Department of Materials Science and Engineering, College of Engineering and Applied Sciences, Jiangsu Key Laboratory of Artificial Functional Materials, Collaborative Innovation Center of Advanced Microstructures, Nanjing University, Nanjing, People's Republic of China

\*Address all correspondence to: [adli@nju.edu.cn](mailto:adli@nju.edu.cn)

## **IntechOpen**

---

© 2021 The Author(s). Licensee IntechOpen. This chapter is distributed under the terms of the Creative Commons Attribution License (<http://creativecommons.org/licenses/by/3.0>), which permits unrestricted use, distribution, and reproduction in any medium, provided the original work is properly cited. 

## References

- [1] Chua L. Memristor-the missing circuit element. *IEEE Transactions on circuit theory*. 1971;18(5):507-519.
- [2] Strukov DB, Snider GS, Stewart DR, Williams RS. The missing memristor found. *nature*. 2008;453(7191):80-83.
- [3] Midya R, Wang Z, Zhang J, Savel'ev SE, Li C, Rao M, et al. Anatomy of Ag/Hafnia-based selectors with  $10^{10}$  nonlinearity. *Advanced Materials*. 2017;29(12):1604457.
- [4] Wang Z, Joshi S, Savel'ev SE, Jiang H, Midya R, Lin P, et al. Memristors with diffusive dynamics as synaptic emulators for neuromorphic computing. *Nature materials*. 2017;16(1):101-108.
- [5] Wang J, Pan R, Cao H, Wang Y, Liang L, Zhang H, et al. Anomalous rectification in a purely electronic memristor. *Applied Physics Letters*. 2016;109(14):143505.
- [6] Du C, Ma W, Chang T, Sheridan P, Lu WD. Biorealistic implementation of synaptic functions with oxide memristors through internal ionic dynamics. *Advanced Functional Materials*. 2015;25(27):4290-4299.
- [7] Azghadi MR, Chen YC, Eshraghian JK, Chen J, Chang YF. Complementary Metal oxide Semiconductor and Memristive Hardware for Neuromorphic Computing. *Advanced Intelligent Systems*. 2020:1900189.
- [8] Kim S, Chen J, Chen YC, Kim MH, Kim H, Kwon M, et al. Neuronal dynamics in  $\text{HfO}_x/\text{AlO}_y$ -based homeothermic synaptic memristors with low-power and homogeneous resistive switching. *Nanoscale*. 2019;11(1):237-245.
- [9] Puurunen RL. Surface chemistry of atomic layer deposition: A case study for the trimethylaluminum/water process. *Journal of applied physics*. 2005;97(12):9.
- [10] Sherman A. Atomic layer deposition for nanotechnology: an enabling process for nanotechnology fabrication: Ivoryton Press; 2009.
- [11] Arden WM. The international technology roadmap for semiconductors —perspectives and challenges for the next 15 years. *Current Opinion in Solid State and Materials Science*. 2002;6(5):371-377.
- [12] Kot M, Das C, Wang Z, Henkel K, Rouissi Z, Wojciechowski K, et al. Room-temperature atomic layer deposition of  $\text{Al}_2\text{O}_3$ : Impact on efficiency, stability and surface properties in perovskite solar cells. *ChemSusChem*. 2016;9(24).
- [13] Cao Y-Q, Zhang W, Xu L, Liu C, Zhu L, Wang L-G, et al. Growth mechanism, ambient stability, and charge trapping ability of Ti-Based maleic acid hybrid films by molecular layer deposition. *Langmuir*. 2019;35(8):3020-3030.
- [14] Yu S, Gao B, Fang Z, Yu H, Kang J, Wong HSP. A low energy oxide-based electronic synaptic device for neuromorphic visual systems with tolerance to device variation. *Advanced Materials*. 2013;25(12):1774-1779.
- [15] Wang L-G, Zhang W, Chen Y, Cao Y-Q, Li A-D, Wu D. Synaptic plasticity and learning behaviors mimicked in single inorganic synapses of  $\text{Pt}/\text{HfO}_x/\text{ZnO}_x/\text{TiN}$  memristive system. *Nanoscale research letters*. 2017;12(1):1-8.
- [16] Mori M, Abegg MH, Gähwiler BH, Gerber U. A frequency-dependent switch from inhibition to excitation in a hippocampal unitary circuit. *Nature*. 2004;431(7007):453-456.



- [17] Liu C, Wang L-G, Cao Y-Q, Wu M-Z, Xia Y-D, Wu D, et al. Synaptic functions and a memristive mechanism on Pt/AlO<sub>x</sub>/HfO<sub>x</sub>/TiN bilayer-structure memristors. *Journal of Physics D: Applied Physics*. 2019;53(3):035302.
- [18] Wang ZQ, Xu HY, Li XH, Yu H, Liu YC, Zhu XJ. Synaptic learning and memory functions achieved using oxygen ion migration/diffusion in an amorphous InGaZnO memristor. *Advanced Functional Materials*. 2012;22(13):2759-2765.
- [19] Jo SH, Chang T, Ebong I, Bhadviya BB, Mazumder P, Lu W. Nanoscale memristor device as synapse in neuromorphic systems. *Nano letters*. 2010;10(4):1297-1301.
- [20] Liu C, Zhang C-C, Cao Y-Q, Wu D, Wang P, Li A-D. Optimization of oxygen vacancy concentration in HfO<sub>2</sub>/HfO<sub>x</sub> bilayer-structured ultrathin memristors by atomic layer deposition and their biological synaptic behavior. *Journal of Materials Chemistry C*. 2020; 8(36):12478-12484.
- [21] Wu C, Kim TW, Guo T, Li F, Lee DU, Yang JJ. Mimicking classical conditioning based on a single flexible memristor. *Advanced Materials*. 2017;29(10):1602890.
- [22] Liu C, Cao Y-Q, Wu D, Li A-D. Simulation of Biologic Synapse Through Organic-Inorganic Hybrid Memristors Using Novel Ti-Based Maleic Acid/TiO<sub>2</sub> Ultrathin Films. *IEEE Electron Device Letters*. 2019;41(1):155-158.
- [23] Zhang W, Kong J-Z, Cao Z-Y, Li A-D, Wang L-G, Zhu L, et al. Bipolar resistive switching characteristics of HfO<sub>2</sub>/TiO<sub>2</sub>/HfO<sub>2</sub> trilayer-structure RRAM devices on Pt and TiN-coated substrates fabricated by atomic layer deposition. *Nanoscale research letters*. 2017;12(1):1-11.
- [24] Pan F, Gao S, Chen C, Song C, Zeng F. Recent progress in resistive random access memories: materials, switching mechanisms, and performance. *Materials Science and Engineering: R: Reports*. 2014;83:1-59.
- [25] Hu L, Zhu S, Wei Q, Chen Y, Yin J, Xia Y, et al. Enhancement of resistive switching ratio induced by competing interfacial oxygen diffusion in tantalum oxide based memories with metal nitride electrode. *Applied Physics Letters*. 2018;113(4):043503.
- [26] Huang C-Y, Huang C-Y, Tsai T-L, Lin C-A, Tseng T-Y. Switching mechanism of double forming process phenomenon in ZrO<sub>x</sub>/HfO<sub>y</sub> bilayer resistive switching memory structure with large endurance. *Applied Physics Letters*. 2014;104(6):062901.
- [27] Kim YJ, Yang BS, Oh S, Han SJ, Lee HW, Heo J, et al. Photobias instability of high performance solution processed amorphous zinc tin oxide transistors. *ACS applied materials & interfaces*. 2013;5(8):3255-3261.
- [28] Wang L-G, Qian X, Cao Y-Q, Cao Z-Y, Fang G-Y, Li A-D, et al. Excellent resistive switching properties of atomic layer-deposited Al<sub>2</sub>O<sub>3</sub>/HfO<sub>2</sub>/Al<sub>2</sub>O<sub>3</sub> trilayer structures for non-volatile memory applications. *Nanoscale research letters*. 2015;10(1):1-8.
- [29] Kim Y-H, Heo J-S, Kim T-H, Park S, Yoon M-H, Kim J, et al. Flexible metal-oxide devices made by room-temperature photochemical activation of sol-gel films. *Nature*. 2012;489(7414):128-132.
- [30] Lian W, Long S, Lü H, Liu Q, Li Y, Zhang S, et al. Approaches for improving the performance of filament-type resistive switching memory. *Chinese Science Bulletin*. 2011;56(4): 461-464.
- [31] Long S, Lian X, Cagli C, Cartoixa X, Rurali R, Miranda E, et al. Quantum-size effects in hafnium-oxide resistive

switching. *Applied Physics Letters*. 2013;102(18):183505.

[32] Kumar S, Wang Z, Huang X, Kumari N, Davila N, Strachan JP, et al. Oxygen migration during resistance switching and failure of hafnium oxide memristors. *Applied Physics Letters*. 2017;110(10):103503.

[33] Chen L, Dai Y-W, Sun Q-Q, Guo J-J, Zhou P, Zhang DW.  $\text{Al}_2\text{O}_3/\text{HfO}_2$  functional stack films based resistive switching memories with controlled SET and RESET voltages. *Solid State Ionics*. 2015;273:66-69.

[34] Long S, Perniola L, Cagli C, Buckley J, Lian X, Miranda E, et al. Voltage and power-controlled regimes in the progressive unipolar RESET transition of  $\text{HfO}_2$ -based RRAM. *Scientific reports*. 2013;3(1):1-8.

[35] Sungjun, Ki, Hyungjin, Kim, Sungmin, Hwang, et al. Analog Synaptic Behavior of a Silicon Nitride Memristor. *ACS Applied Materials & Interfaces*. 2017;9(46).

[36] Yu S, Wu Y, Jeyasingh R, Kuzum D, Wong H-SP. An electronic synapse device based on metal oxide resistive switching memory for neuromorphic computation. *IEEE Transactions on Electron Devices*. 2011;58(8):2729-2737.

[37] Huang XD, Li Y, Li HY, Xue KH, Miao XS. Forming-Free, Fast, Uniform, and High Endurance Resistive Switching From Cryogenic to High Temperatures in  $\text{W}/\text{AlO}_x/\text{Al}_2\text{O}_3/\text{Pt}$  Bilayer Memristor. *IEEE Electron Device Letters*. 2020;PP(99):1-.

[38] Yan X, Qin C, Lu C, Zhao J, Li H. Robust  $\text{Ag}/\text{ZrO}_2/\text{WS}_2/\text{Pt}$  Memristor for Neuromorphic Computing. *ACS Applied Materials & Interfaces*. 2019;11:48029-48038.